Materials Horizons

ROYAL SOCIETY OF CHEMISTRY

COMMUNICATION

View Article Online
View Journal | View Issue

Cite this: *Mater. Horiz.*, 2020, 7, 1809

Received 6th February 2020,
Accepted 27th April 2020

DOI: 10.1039/d0mh00197j

rsc.li/materials-horizons

Computational discovery of promising new n-type dopable ABX Zintl thermoelectric materials†

Prashun Gorai, *[a] Alex Ganose, [b] Alireza Faghaninia, [b] Anubhav Jain[b] and Vladan Stevanović[a]

Computational prediction of good thermoelectric (TE) performance in several n-type doped Zintl phases, combined with successful experimental realization, has sparked interest in discovering new n-type dopable members of this family of materials. However, most known Zintls are typically only p-type dopable; prior successes in finding n-type Zintl phases have been largely serendipitous. Here, we go beyond previously synthesized Zintl phases and perform chemical substitutions in known n-type dopable ABX Zintl phases to discover new ones. We use first-principles calculations to predict their stability, potential for TE performance as well as their n-type dopability. Using this approach, we find 17 new ABX Zintl phases in the KSnSb structure type that are predicted to be stable. Several of these newly predicted phases (KSnBi, RbSnBi, NaGeP) are found to exhibit promising n-type TE performance and are n-type dopable. We propose these compounds for further experimental studies, especially KSnBi and RbSnBi, which are both predicted to be good TE materials with high electron concentrations due to self-doping by native defects, when grown under alkali-rich conditions.

New concepts

We develop the chemical replacements in structure prototype (CRISP) approach for novel materials discovery with functional applications. Typically, computational searches of functional materials focus on known compounds in crystallographic databases, ignoring the large phase space of unexplored chemistries containing potentially breakthrough materials. For example, whereas the majority of known Zintl phases can only be doped p-type, there exists an opportunity to discover yet-unknown n-type Zintl thermoelectrics. We employ a CRISP search across a large chemical space to identify stable but unreported ABX Zintl phases with high predicted n-type thermoelectric performance. Starting from a prototype with confirmed high thermoelectric performance and n-type dopability, we explore approximately 4,900 candidate materials and discover 17 unreported Zintl phases that show promise as n-type thermoelectrics. Surprisingly, several of our predictions exhibit even greater potential for n-type doping than our initial prototype. The CRISP approach offers new opportunities to explore previously unknown compounds with desired functional and doping behaviour and can be exploited for many applications beyond thermoelectrics.

1 Introduction

Since the pioneering work by Eduard Zintl, and later by Wilhelm Klemm, Zintl phases have intrigued solid-state chemists because of their unique chemical bonding and structural features.[1,2] Zintl phases are typically composed of electropositive cations (alkali, alkaline earth, rare-earths) that are ionically bonded to frameworks formed of covalently-bonded polyanions.[3,4] The electron counting in these valence-precise compounds conform to the 8-*N* rule explained by the Zintl–Klemm concept.[5,6]

A good thermoelectric (TE) material is a semiconductor that possesses high electronic conductivity, large Seebeck coefficient, and low thermal conductivity. Many Zintl phases fulfill these criteria owing to their small band gaps,[7] dispersive bands, and loosely bound cations.[8] Indeed, Zintl phases such as $Yb_{14}MnSb_{11}$,[9] $CaZn_2Sb_2$,[10] Sr_3GaSb_3,[11] and $Ca_5Al_2Sb_6$[12] are among the best performing thermoelectric materials. A peculiar characteristic of these well-known TE materials, as well as other Zintl phases, is that they are all natively p-type with moderate to high hole concentrations due to self-doping. Only a few members of this material family have been found to be n-type dopable.

It was computationally predicted that many Zintls phases, if doped n-type, will exhibit comparable, or even better TE performance, than their p-type counterparts.[13,14] Subsequent experimental demonstration of good thermoelectric performance in n-type Zintl phases[13,15] have endorsed these theoretical predictions and sparked a widespread interest in discovering n-type dopable Zintl phases. The discovery of new n-type Zintl phases has been largely fortuitous while chemical strategies to discover such new phases remain elusive. Materials discovery enabled by computations have been fairly successful in identifying novel materials for various applications.[16–23] However, in general,

[a] *Colorado School of Mines, Golden, CO 80401, USA. E-mail: pgorai@mines.edu, vstevano@mines.edu*

[b] *Lawrence Berkeley National Laboratory, Berkeley, CA 94720, USA*

† Electronic supplementary information (ESI) available. See DOI: 10.1039/d0mh00197j

computational searches have focused on known materials taken from crystallographic databases.

Given the fundamental challenges of finding Zintl phases that can be doped n-type, it might be prudent to think out of the "box" of known materials. To this end, there are a plethora of chemically plausible Zintl phases that are likely stable and worth exploring but have not yet been synthesized. If the structure and chemistry of the new Zintl phases are judiciously chosen, such an exploration may reveal stable phases that are dopable n-type and also exhibit high thermoelectric performance. One route to finding stable, n-type dopable high-performing thermoelectric Zintl phases is by chemical replacements in structure prototype (CRISP).[24,25] Within the CRISP approach, we begin with a known Zintl phase that is proven to be n-type dopable and exhibits good thermoelectric performance. This known Zintl phase serves as a structure prototype; chemical replacements in the prototypical structure are used to generate new Zintl phases, which are then assessed for stability, thermoelectric performance, and desired dopability. We hypothesize that the n-type dopability and the promising TE performance are features of the crystal structure that will be translated to other chemistries. In that sense, the CRISP approach represents an "informed" search, which increases the likelihood of finding promising candidates. As we will show later, our calculations largely validate this hypothesis. The computational community has long been concerned about limiting the search for functional materials to crystallographic databases; several computational efforts to explore as-yet-unknown materials have been reported in the last decade.[24–30]

In this work, we employ the CRISP approach to explore ABX Zintl phases (A = Li, Na, K, Rb, Cs; B = Si, Ge, Sn, Pb, Zn, Cd; X = P, As, Sb, Bi) in the KSnSb structure prototype (Fig. 1). The hexagonal crystal structure of KSnSb ($P6_3mc$) contains corrugated Sn–Sb layers interspersed with K. Given the small electronegativity difference between Sn and Sb ($\Delta\chi_{Sn-Sb}$ = 0.09 on Pauling scale), the Sn–Sb intra-layer bonds have significant covalent character. In contrast, K is highly electropositive ($\Delta\chi_{K-Sb}$ = 1.23) and therefore, donates electron to the Sn–Sb layered anionic framework. As such the Zintl–Klemm concept can be invoked to rationalize the composition–structure relationship in KSnSb. The primary reasons for exploring the KSnSb prototype structure are three-fold: (1) our previous work[31] as well as subsequent theoretical studies[32,33] have predicted high thermoelectric performance for n-type KSnSb, (2) our defect calculations reveal that KSnSb is n-type dopable (see Section 3), and (3) the chemical space of ABX Zintls seem to be under-explored (see Section 3), making it likely to contain undiscovered Zintl phases. Discovery of new ABX compounds has been the subject of past computational efforts,[24,25,34–36] however, those studies have primarily focused on 18-electron half-Heuslers, which are distinct from the ABX Zintl phases considered here.

Out of the 140 ABX compositions considered in this work, 24 are known phases reported in the Inorganic Crystal Structure Database (ICSD).[37] Of the remaining 116 compositions, we find that 17 should be stable – structurally (in the KSnSb prototype structure *versus* other competing ABX structures) and compositionally (lie within 20 meV per atom from the convex hull). We also find these 17 ABX phases to be dynamically stable, with regard to the absence of imaginary phonon frequencies at Γ. In addition, these 17 ABX phases have non-zero, small (<1 eV) DFT band gaps and 14 of them are predicted to exhibit high n-type TE performance. We perform first-principles defect calculations for 5 candidate phases to assess their n-type dopability. We also report 28 other undiscovered ABX Zintl phases (stable in structures other than the KSnSb prototype) that are equally interesting and warrant further investigation.

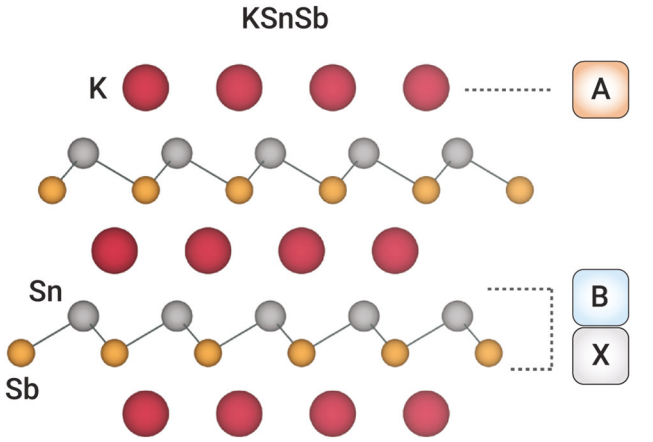

Fig. 1 Hexagonal crystal structure of KSnSb composed of corrugated Sn–Sb layers interspersed with K. We perform CRISP (see text for details) using KSnSb prototype structure, where A is replaced with Li, Na, K, Rb, Cs, B with Si, Ge, Sn, Pb, Zn, Cd, Be and X with P, As, Sb, Bi.

2 Computational methods

Fig. 2 summarizes the computational workflow. First, we relax the hypothetical structures created by chemical replacements in structure prototype (CRISP). Compositions that retain the prototype structure (KSnSb in this study), as determined by the space group, are assessed for their compositional, structural, and dynamic stability. Subsequently, we predict the thermoelectric performance of those compositions that are stable and have non-zero DFT band gaps. Finally, we assess the n-type dopability of the top candidates.

2.1 Structure relaxation

Structures created by chemical replacements in structure prototypes (CRISP) are relaxed with density functional theory (DFT) using the plane-wave VASP code.[38] The generalized gradient approximation (GGA) in the Perdew–Burke–Ernzerhof (PBE)[39] functional form is used within the projector augmented wave (PAW) formalism.[38] For structural relaxations, a procedure similar to that used in ref. 15 and 40 is employed, with a plane-wave energy cutoff of 520 eV and a Monkhorst–Pack *k*-point sampling. Non spin-polarized calculations are performed since elements A, B, and X, including Zn and Cd, are typically non-magnetic. Structural relaxations are performed in

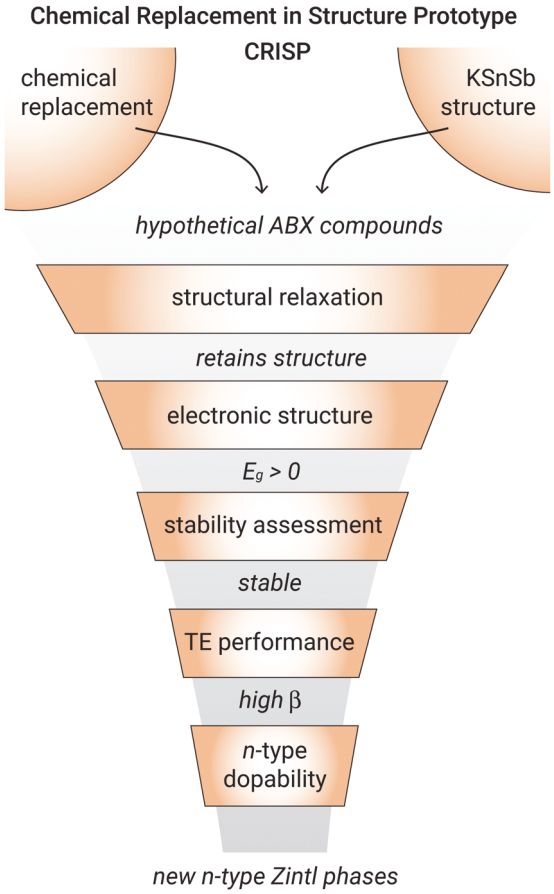

Fig. 2 Schematic workflow of chemical replacements in structure prototype (CRISP) approach. We employ the CRISP approach to discover new n-type dopable ABX Zintl phases in the KSnSb prototype structure. Here, E_g is band gap and β is the predicted thermoelectric quality factor, a measure of thermoelectric performance.

a high-throughput approach with the aid of the pymatgen,[41] FireWorks,[42] and atomate[43] software packages.

2.2 Stability

Structural. To assess structural stability, we consider each of the 140 ABX compositions in 35 different structure types. This includes the 8 known structures adopted by the ABX Zintl phases (KSnSb, NaCdSb, NaZnSb, LiZnSb, LiSnSb, KZnSb, KZnP, LiZnAs). The remaining 27 structure types are selected from all ICSD structures that possess 1-1-1 ternary stoichiometries. The complete list of 35 structures is provided in the ESI.† For instance, we consider the prototypical half-Heusler structure (NiMnP, $F\bar{4}3m$) as one of the possible structures. We consider ternary structures ranging from low (*e.g.* KCN in *Cc* and *Cm* structures) to high (*e.g.* CoMnSb $Fm\bar{3}m$) symmetry. To assess structural stability, each ABX composition is substituted in the 35 different structure types, the structures are fully relaxed with DFT and their total energies are calculated. For a given ABX composition, the structure with the lowest energy is deemed to be the most favorable. As a validation, we find that the 8 known ABX Zintl phases are the most stable in their respective structure types.

Compositional. The stability of each composition is assessed using the convex hull construction, which provides the stability of a compound against decomposition into competing phases. Stable phases lie on the convex hull while unstable and metastable phases lie above the hull; the energy above the hull is an indicator of phase stability. We evaluated the compositional stability of the ABX compounds that have non-zero calculated band gap. The convex hull construction is performed using the total energies of competing phases documented in the Materials Project[44,45] using the phase diagram construction in pymatgen.[46]

Dynamic. A general method for assessing the dynamic stability of structures is by calculating the full phonon dispersion to determine the presence of imaginary frequencies ($\omega^2 < 0$). The presence of imaginary phonon frequency is an indicator of dynamic instability.[47] However, calculation of full phonon dispersion is computationally expensive and not amenable to high-throughput assessment. Since long-wavelength (small $\vec{q}$ vector) dynamic instabilities are the most common,[48] we assess the stability by computing phonon dispersion at Γ using density functional perturbation theory (DFPT) as implemented in the VASP code.[38] To obtain accurate descriptions of the atomic forces, the structures are re-relaxed using a tight force convergence criteria of 5×10^{-4} eV Å^{-1}. A large plane-wave cutoff energy of 700 eV is utilized along with an energy convergence tolerance of 10^{-8} eV. While it is possible that imaginary frequency modes exist at q points other than Γ, such instabilities are less common. We find that all ABX compositions in their predicted stable structures are dynamically stable at Γ.

2.3 Metric for thermoelectric performance

We computationally assess the potential for thermoelectric performance using a previously developed descriptor – quality factor β (see ref. 31 for details), which is defined as:

$$\beta \propto \frac{\mu_0 {m_{\mathrm{DOS}}}^{*3/2}}{\kappa_{\mathrm{L}}} T^{5/2} \quad (1)$$

where μ_0 is the intrinsic charge carrier mobility (300 K), m_{DOS}* the density-of-states (DOS) effective mass, κ_{L} the lattice thermal conductivity (300 K), and T is the temperature. The higher the value of β, the better the predicted TE performance. To address the challenges associated with direct calculation of transport properties, μ_0 and κ_{L} are calculated using semi-empirical models that were developed by combining DFT calculations and measured room-temperature μ_0 and κ_{L} for a range of materials.[31] To determine β one needs to calculate m_{DOS}*, band effective mass m_{b}*, and bulk modulus B.

Electronic structures are calculated on a dense k-point grid with a fixed number of k-points, as determined by the equation $N_{\mathrm{atoms}} \times N_{\mathrm{kpts}} \simeq 8000$, where N_{atoms} is the number of atoms in the primitive cell and N_{kpts} the number of k-points. This k-point density is equivalent to a $16 \times 16 \times 16$ k-point grid for diamond-Si and provides sufficiently converged electronic structure parameters such as band gaps and effective masses. m_{DOS}* is determined from the DOS within the parabolic band approximation, such that the parabolic band reproduces the

same number of states as the DOS within a 100 meV energy window from the relevant band edges. The band effective mass is determined from m_{DOS}^* and band degeneracy N_b by assuming spherical and symmetric carrier pockets and using the relationship $m_b^* = m_{DOS}^* N_b^{-2/3}$. B is calculated by fitting the Birch–Murnaghan equation of state[49] to a set of total energies computed at different volumes.

2.4 Defect energetics

The formation energetics of point defects can be reliably calculated with standard methods such as the supercell approach.[15,50,51] The defect formation energy is calculated as:

$$\Delta E_{D,q} = (E_{D,q} - E_H) + qE_F + \sum_i n_i\mu_i + E_{corr} \qquad (2)$$

where $E_{D,q}$ and E_H are the total energies of the supercell containing defect D in charge state q and the defect-free host supercell, respectively. E_F is the Fermi energy and E_{corr} comprises all the finite-size corrections that are applied within the supercell approach.[50] The dependence of the formation energy on the phase stability and growth conditions is captured by the term $\sum_i n_i\mu_i$. The chemical potential of element i is denoted by μ_i and n_i is the number of atoms of element i added ($n_i < 0$) or removed ($n_i > 0$) from the supercell. Conventionally, the elemental chemical potential μ_i is expressed relative to the reference elemental phase as $\mu_i = \mu_i^0 + \Delta\mu_i$, where μ_i^0 is the reference chemical potential under standard conditions and $\Delta\mu_i$ is the deviation from the reference chemical potential. $\Delta\mu_i = 0$ corresponds to i-rich growth conditions while large negative values of $\Delta\mu_i$ correspond to i-poor growth conditions. The bounds on $\Delta\mu_i$ for a given material are set by the region of phase stability.

First-principles defect calculations are performed with density functional theory (DFT) in the generalized gradient approximation of Perdew–Burke–Ernzerhof (PBE),[39] utilizing the projector augmented wave (PAW) formalism as implemented in the VASP software package.[38] Defect energetics are calculated using the standard supercell approach.[50] The total energies of 96-atom defect supercells are calculated with a plane-wave energy cutoff of 340 eV and a Γ-centered $4 \times 4 \times 4$ Monkhorst–Pack k-point grid to sample the Brillouin zone. The defect supercells are relaxed following the procedure used in ref. 15 and 52. Typically, DFT-calculated total energies (0 K) of elemental phases are used as reference elemental chemical potentials (μ_i^0), which can lead to erroneous formation enthalpies.[53] Inspired by the fitted elemental-phase reference energies (FERE) approach,[53] the reference chemical potentials (see ESI†) are obtained by fitting to a set of experimentally measured formation enthalpies.

The underestimation of band gaps in DFT-GGA is remedied by applying band edge shifts as determined from GW quasiparticle energy calculations, following the procedure previously employed in ref. 15 and 52. The band gap correction also includes band edge shifts arising from spin–orbit coupling (SOC) calculated on the PBE-relaxed structures. The following corrections are included in E_{corr}, following the state-of-the-art methodology described in ref. 50: (1) image charge correction for charged defects, (2) potential alignment correction for charged defects, (3) band filling correction for shallow defects, and (4) band gap correction for shallow acceptors/donors. The calculation setup and analyses are performed using a software package, pylada-defects, that we have developed to automate point defect calculations.[54]

For a given material, the defect formation energies of all vacancies, antisites, and interstitials are calculated in charge states q = −3, −2, −1, 0, 1, 2, and 3. In most materials considered in this study, the formation energy of interstitials is relatively high. Vacancies and antisite defects derived from all unique Wyckoff positions in the crystal structure are included in the calculations. The most likely interstitial sites are automatically identified *via* a Voronoi tessellation scheme as implemented in pylada-defects.[54] For KSnSb, we considered K and Sn interstitials in 10 different possible sites. Similarly, we considered K, Sn interstitials in KSnBi (9 sites), Sn intersitials in RbSnBi (9 sites), Na, Ge interstitials in NaGeP (8 sites), and K interstitials in KGeP (10 sites). The relaxed structures of the most favorable interstitial sites in KSnSb, KSnBi, RbSnBi, NaGeP, and KGeP in their relevant charge states are shown in Fig. S1 in the ESI.†

3 Results and discussion

3.1 Known compounds in the chemical search space

To search for new ABX Zintl phases in the KSnSb prototype structure, we adopted the CRISP approach by considering five A^+ ions (Li, Na, K, Rb, Cs), seven B^{2+} ions (Si, Ge, Sn, Pb, Zn, Cd, Be), and four X^{3-} pnictides (P, As, Sb, Bi). The choice of elements A, B, and X are based on the formal oxidation states and electronegativity considerations ($\Delta\chi_{B-X}$, $\Delta\chi_{A-B,X}$), as explained in the Introduction. Out of the 140 ABX compositions considered in this study, 24 are known compounds reported in the ICSD, as summarized in Fig. 3. These 24 compounds are reported in 8 distinct prototypical structures – NaCdSb (*Pnma*, 62), NaZnSb (*P*4/*nmm*, 129), LiZnSb ($P6_3mc$, 186), KSnSb ($P6_3mc$, 186), LiSnSb ($P6_3mc$, 186), KZnSb ($P\bar{6}m2$, 187), KZnP ($P6_3/mmc$, 194), LiZnAs ($F\bar{4}3m$, 216), where space group names and numbers are specified in parentheses. The crystal structures are shown in Fig. S2 in the ESI.†

Inspection of known ABX compounds in Fig. 3: (1) suggests an apparent lack of systematic investigation of ABX compounds within the considered chemical search space, and (2) reveals the complete absence of bismuthides (X = Bi). Based on chemical intuition, it appears that the chemical search space in Fig. 3 is under-explored. For instance, consider LiZnP, LiCdP, LiBeP, LiZnAs, LiCdAs, LiBeAs and LiZnSb, LiCdSb, LiBeSb: all, except LiCdSb, are known phases. Therefore, one would expect from chemical intuition that LiCdSb should be a stable phase (it is indeed! see Section 3.2) but it has not been reported in the ICSD. LiCdSb has been investigated as part of a computational study.[55] Similarly, it seems quite surprising that

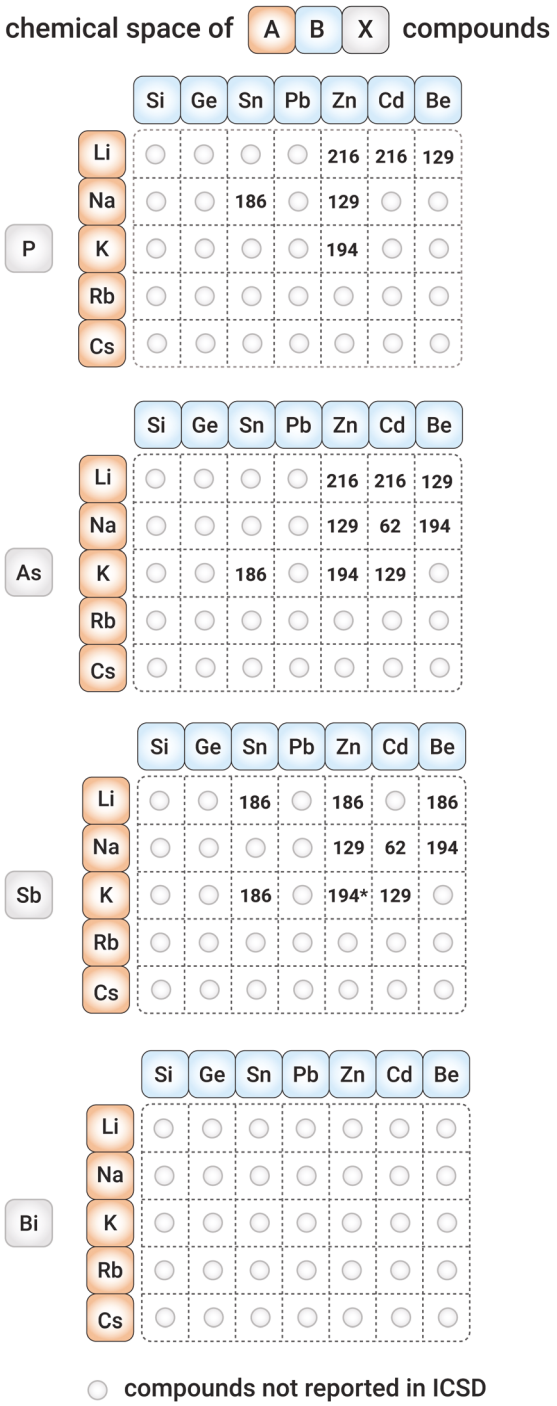

Fig. 3 The chemical search space of ABX Zintl phases, where A (alkali) = Li, Na, K, Rb, Cs; B = Si, Ge, Sn, Pb, Zn, Cd, Be; and X (pnictide) = P, As, Sb, Bi. Among the 140 possible chemistries, 24 compounds are reported in the ICSD, denoted by their space group numbers. The circles correspond to ABX chemistries that are not reported in the ICSD. *KZnSb has two different structures – ground state (194) and a higher-energy phase (187).

none of the bismuthide phases have been discovered. Within Zintl pnictides, it is not uncommon for both antimonide and bismuthide phases to exist. Examples include Mg_3Sb_2 and Mg_3Bi_2,[56] $Yb_{14}MnSb_{11}$ and $Yb_{14}MnBi_{11}$,[9] KSb and KBi,[40] and CsSb and CsBi.[40] With underexploration comes opportunities. Therefore, the chemical space considered in this study presents a fertile search landscape to discover new ABX Zintl phases.

3.2 Stability of predicted compounds

The 140 ABX compositions in the KSnSb prototype structure were relaxed following the procedure described in Section 2.1. We find that all 140 compositions retain the symmetry of the prototype after the initial relaxation. For each of these 140 compositions, we assessed their structural stability using the methodology described in Section 2.2. We find that 20 ABX compositions are most stable in the KSnSb structure type and lie either on (14) or within 20 meV per atom (6) from the convex hull (Fig. 4). The 6 compounds that lie within 20 meV per atom of the hull could be deemed compositionally stable due to the typical DFT prediction errors.[45,53,57] The 20 ABX compounds that are stable in the KSnSb prototype structure include known compounds (KSnSb, NaSnP, KSnAs) and 17 previously unreported materials (NaGeP, KGeP, KSnP, LiPbAs, NaGeAs, NaSnAs, NaPbAs, KGeAs, KPbAs, RbGeAs, RbSnAs, RbPbAs, RbSnSb, CsSnSb, KSnBi, RbSnBi, CsSnBi). We further find that these 20 compounds are dynamically stable at Γ (see Section 2.2).

In addition to the 17 unreported ABX compositions that are stable in the KSnSb structure type, our predictions suggest that there are an additional 28 undiscovered ABX compositions that are stable in other structure types (Fig. 5). The complete list of 45 newly predicted ABX Zintl phases and their energy above the convex hull are reported in the ESI† (Table S1). These newly predicted compounds comprise 13 phosphides, 17 arsenides, 8 antimonides, and 7 bismuthides (Fig. 5). A survey of the published literature using Matscholar (www.matscholar.com)[58] further confirms that these 45 compounds are indeed new and previously unreported (except LiCdSb[55]). The larger number of undiscovered arsenides could be due to synthesis challenges associated with handling As, which is toxic. Among the 24 known ABX phases, there are none that contain Rb or Cs. Our predictions suggest that 27 ABX phases (6 phosphides, 10 arsenides, 7 antimonides, 4 bismuthides) where cation A is Rb or Cs should be stable. Again, we speculate that Rb and Cs containing ABX phases have not been discovered due to synthetic challenges of handling air-sensitive Rb and Cs. However, there are

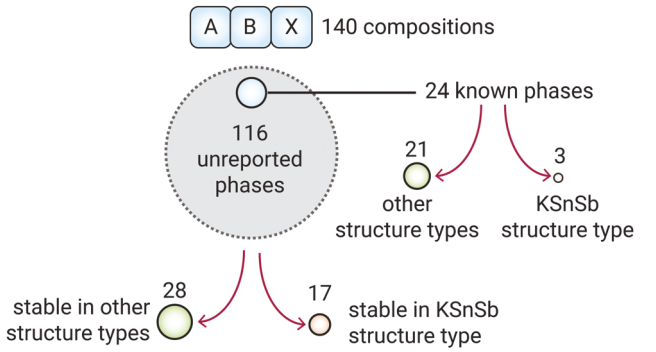

Fig. 4 Statistics of ABX Zintl phases: out of 140 compositions considered, 24 are known phases and 45 are predicted to be stable, including 17 in KSnSb structure type and 28 in other structure types.

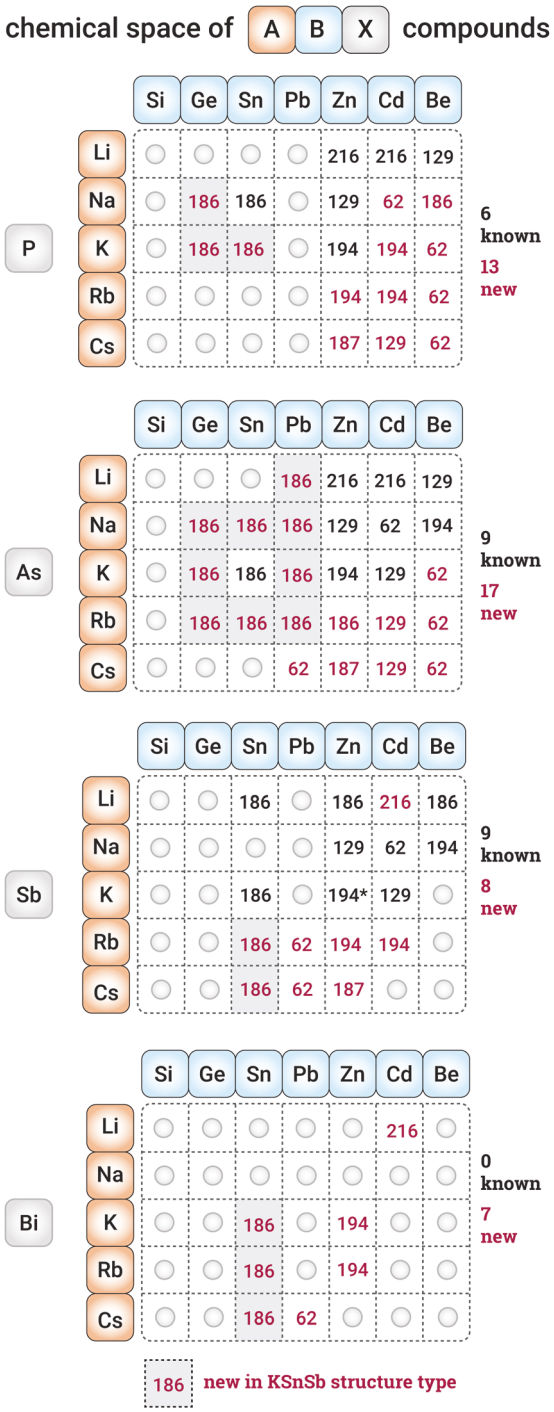

Fig. 5 Search space of 140 ABX chemistries marked with known ICSD (black) and newly reported (red) compounds. The compounds are denoted by their space group numbers. We predict 45 new ABX phases, comprising 13 phosphides, 17 arsenides, 8 antimonides, and 7 bismuthides. Of these, 17 phases are predicted to be stable in the KSnSb prototype structure (shaded).

well-known, high-performing thermoelectric materials such as $CsBi_4Te_6$.[59] As such, it is worth exploring even Rb- and Cs-containing ABX Zintl phases for thermoelectrics, despite their potential air sensitivity and associated synthetic challenges.

3.3 Predicted thermoelectric performance

Fig. 6 shows the computed intrinsic electron mobility (μ_e) as a function of lattice thermal conductivity (κ_L) for the 69 stable Zintl phases (Fig. 4). The marker size denotes the value of n-type β (larger β correspond to higher predicted TE performance). Most of the ABX compounds exhibit relatively low κ_L <5 W m^{-1} K^{-1}, with the largest n-type β compounds lying in $\sim$1–5 W m^{-1} K^{-1} regime.

We now turn our focus to a subset of the data points in Fig. 6 – the 20 ABX compounds (blue markers) that are predicted to be stable in the KSnSb prototype structure. The predicted transport properties and TE performance of these 20 stable phases are summarized in Table 1. The prototype material KSnSb has the largest n-type β while 11 compounds have normalized n-type $\beta/\beta_{PbTe} > 1$. The large n-type β values of the 11 compounds generally stem from their low lattice thermal conductivities (κ_L), large CB degeneracy (N_b), and low CB effective masses ($m_{b,CB}$*). The large conduction band $N_b = 7$ of KSnSb can be gleaned from the electronic structure (Fig. S3, ESI†). Within 100 meV from the conduction band minimum, there are two bands – one at Γ ($N_b = 1$) and another along Γ–M ($N_b = 6$). The low κ_L can be attributed to the presence of low-lying optical modes in the phonon dispersion (Fig. S4, ESI†), which allow increased scattering of acoustic modes.[60]

It is notable that many of the large β compounds in Fig. 6 are those that prefer to adopt the KSnSb prototype structure. The high predicted TE performance of the ABX compounds in the KSnSb structure demonstrates that the CRISP approach, which is "informed" by prototypes with desired properties, increases

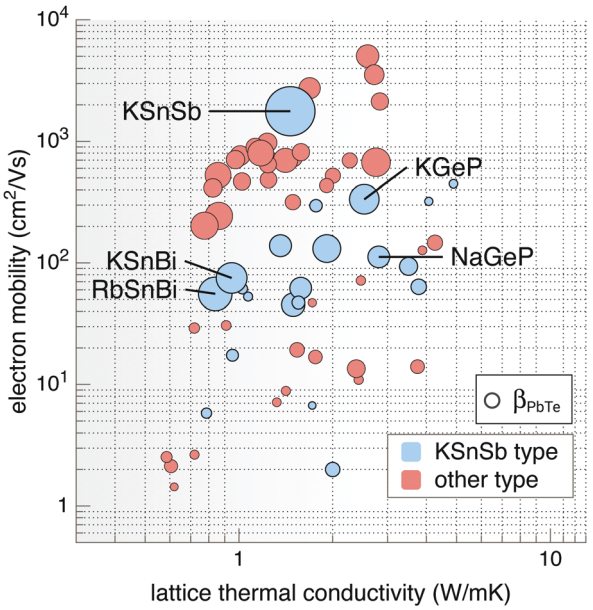

Fig. 6 Calculated n-type quality factor (β), denoted by the marker size, plotted as a function of the computed electron mobility and lattice thermal conductivity. For reference, the marker size corresponding to the β value of PbTe is shown as a legend. The color scheme denotes the stable structure type. The n-type dopability of the labelled compounds is assessed with defect calculations (Fig. 7).

Table 1 Computed electronic structure and transport properties, and thermoelectric performance of 20 ABX Zintl phases that are predicted to be stable in the KSnSb structure type. ΔE_{hull} is the energy above the convex hull (in meV per atom), $m_{b,CB}$* is conduction band effective mass (in m_e), κ_L is lattice thermal conductivity (in W m^{-1} K^{-1}), μ_n is electron mobility (in cm^2 V^{-1} s^{-1}), and β_n/β_{PbTe} is normalized n-type TE quality factor (unitless)

Compound	ΔE_{hull} (meV)	$m_{b,CB}$* (m_e)	κ_L (W m^{-1} K^{-1})	μ_n (cm^2 V^{-1} s^{-1})	β_n/β_{PbTe}
KSnSb[a]	0	0.014	1.46	1772	12.5
RbSnBi	0	0.117	0.84	56	5.8
KSnBi	2	0.104	0.95	75	4.8
KGeP	4	0.054	2.53	334	4.5
NaGeAs	0	0.098	1.91	131	4.0
KPbAs	0	0.141	1.49	45	2.8
LiPbAs	6	0.096	1.36	139	2.5
NaGeP	0	0.124	2.81	112	2.4
NaPbAs	0	0.124	1.58	62	2.4
NaSnAs	0	0.107	3.51	94	1.7
NaSnP[a]	1	0.151	3.78	64	1.2
RbGeAs	4	0.176	1.55	47	0.8
KGeAs	16	0.053	1.77	296	0.8
CsSnSb	0	0.263	0.95	17	0.7
RbSnSb	0	0.115	1.02	61	0.6
CsSnBi	0	0.518	0.79	6	0.5
RbSnAs	0	0.101	1.07	53	0.4
KSnAs[a]	0	0.045	4.88	448	0.4
KSnP	0	0.048	4.07	322	0.3
RbPbAs	0	0.524	1.72	7	0.3

[a] Known ABX phases in KSnSb structure type.

the likeliness of finding promising, undiscovered materials with similar properties. While the focus of this work is on discovering new n-type dopable Zintl phases, it is also worth examining the p-type performance of these phases. The normalized p-type β/β_{PbTe} of all 20 stable compounds listed in Table 1 are <1; for the prototype compound KSnSb, the value is 0.5. Therefore, we see that the expected properties of compounds discovered *via* the CRISP approach tend to reflect not only the expected n-type but also the p-type TE performance.

3.4 n-Type dopability of candidate materials

The discovery of n-type ABX Zintl phases *via* the CRISP approach hinges on the fact that the prototype material (KSnSb) is dopable n-type. Fig. 7a shows the formation energetics of the native defects in KSnSb grown under the most K-rich conditions within the phase stability region. Defects with negative slopes are acceptors while those with positive slopes are donors. In KSnSb, anti-site Sb_{Sn} is the only low-energy native donor defect. Under K-rich growth conditions, the anti-site Sn_{Sb} is the lowest-energy acceptor defect. The well-known p-type self-doping of many Zintl phases, including $Ca_5Al_2Sb_6$ and $SrZn_2Sb_2$, is due to the low formation energy of the cation vacancies. Therefore, KSnSb is somewhat peculiar in its defect behavior compared to other well-known Zintl phases. Under the most K-rich conditions (Fig. 7a), KSnSb is natively p-type doped by the acceptor anti-site defect Sn_{Sb}. However, the slightly higher formation energy of that anti-site defect leaves the opportunity to possibly dope KSnSb n-type by introducing extrinsic donor dopants. The n-type dopability can be gauged from ΔE_{don} – the energy window at the conduction band minimum created by the lowest-energy acceptor defect under the given growth condition. The larger the ΔE_{don} window, the greater the opportunity for n-type doping. If ΔE_{don} is negative, the equilibrium Fermi energy due to extrinsic donor doping will lie in the band gap; degenerate doping, which is typically needed to maximize thermoelectric performance, cannot be achieved in this case. For KnSnSb, the largest ΔE_{don} window ($\sim$0.3 eV) is under the growth conditions shown in Fig. 7a. The positive, but somewhat small, value of ΔE_{don} suggest that KSnSb could be degenerately doped n-type provided a suitable extrinsic donor dopant is available. Together, the predicted high n-type TE performance and dopability, makes KSnSb a suitable structure prototype to discover new Zintl phases *via* the CRISP approach.

We selected four newly predicted compounds from the candidate materials listed in Table 1 and performed defect calculations to assess their n-type dopability. The formation energetics of the native defects in KSnBi, RbSnBi, NaGeP, and KGeP are shown in Fig. 7b–e, respectively, under the most alkali-rich conditions as allowed by the phase stability region of each compound. In selecting the four compounds for defect calculations, we avoided toxic As-containing phases even though the predicted TE performance is relatively high for NaGeAs, KPbAs, NaSnAs *etc.* (Table 1). Given the absence of known bismuthides among the investigated ABX Zintl phases (Fig. 3), combined with their large β values (Table 1), we chose to examine KSnBi and RbSnBi. Within thermoelectrics, arsenide, antimonide, and bismuthide Zintl phases are common but phosphides are relatively scarce. For this reason, we selected NaGeP and KGeP for performing defect calculations. Additionally, phosphides are earth-abundant and non-toxic material. We found KSnBi, RbSnBi, and NaGeP to be n-type dopable; the electronic structures and phonon dispersions of these three Zintl phases are provided in Fig. S3 and S4, respectively, of the ESI.† The absence of imaginary modes in the phonon dispersions of KSnBi, RbSnBi, and NaGeP further confirm their dynamic stability.

KSnBi. The formation energetics of native defects in KSnBi are shown in Fig. 7b under K-rich growth conditions, which maximizes the n-type dopability window (ΔE_{don}). Like KSnSb, the lowest-energy acceptor under these conditions is the anti-site defect Sn_{Bi}, as opposed to the cation vacancy V_K. The high formation energy of Sn_{Bi} creates a large $\Delta E_{don} \sim 0.48$ eV, making KSnBi an n-type dopable phase. In fact, the low formation energy of the donor Bi_{Sn} defect ensures that KSnBi is degenerately doped n-type even without the introduction of extrinsic dopants. The predicted free electron concentration at 500 °C (typical growth temperature of ABX Zintl phases[61]) under K-rich conditions is 9.9×10^{19} cm^{-3}. Therefore, KSnBi is an exciting candidate Zintl phase with predicted high TE performance and high free electron concentration due to n-type self-doping under alkali-rich growth conditions.

RbSnBi. The native defect energetics in RbSnBi (Fig. 7c) are similar to that of KSnBi. The lowest-energy native acceptor defect is Sn_{Bi}; the high formation energy of Sn_{Bi} creates a large n-type dopability window $\Delta E_{don} \sim 0.42$ eV. Compared to KSnBi, ΔE_{don} is slightly smaller, which could be an effect of the larger

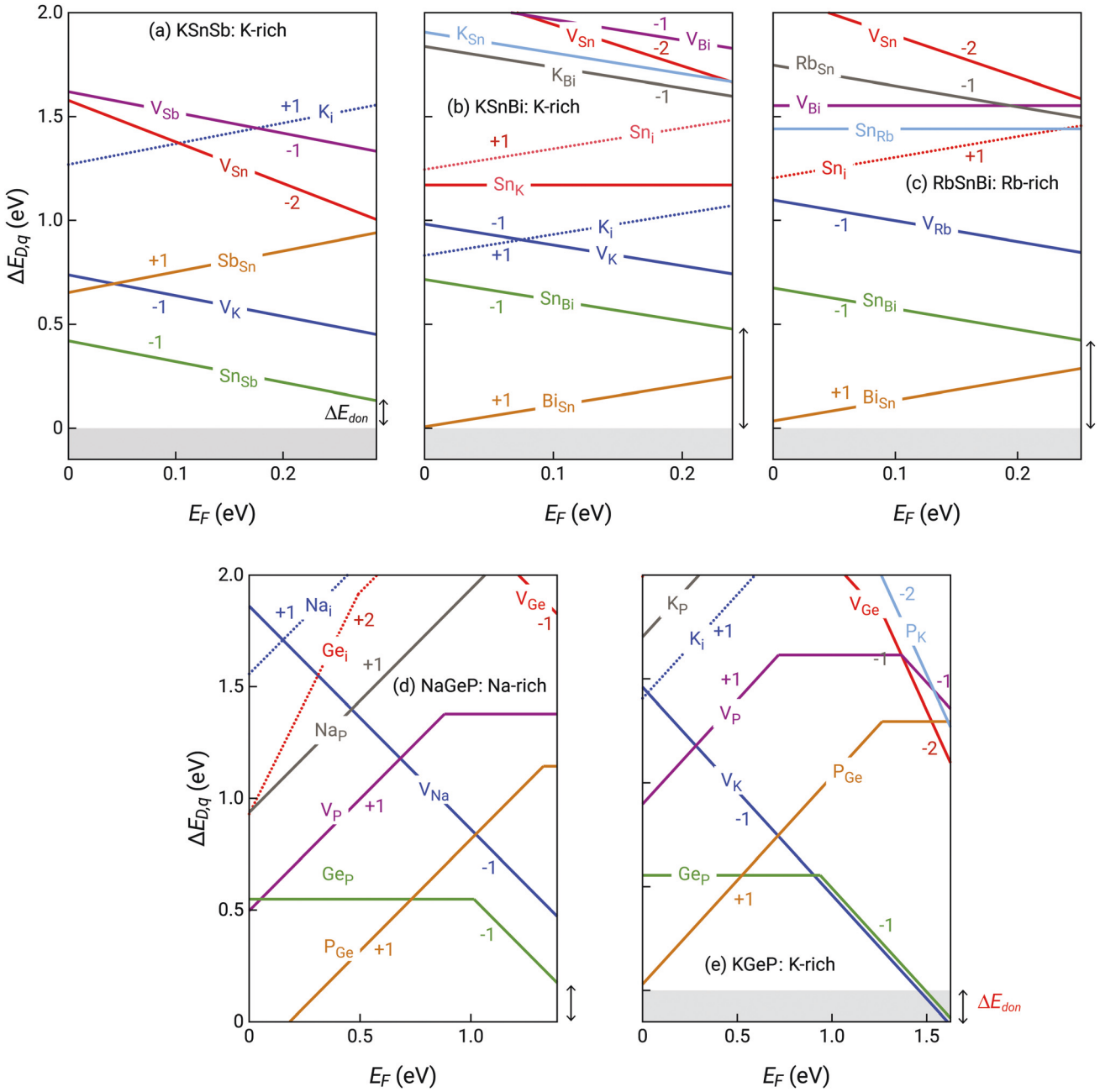

Fig. 7 Formation energies of native defects ($\Delta E_{D,q}$) as functions of Fermi energy (E_F) for (a) KSnSb (under K-rich conditions), (b) KSnBi (under K-rich condition), (c) RbSnBi (under Rb-rich condition), (d) NaGeP (under Na-rich condition), and (e) KGeP (under K-rich condition). E_F is referenced to the valence band maximum. The upper limit of E_F shown is the conduction band minimum such that E_F values range from 0 to the band gap. The lowest-energy acceptors are anti-site defects, except in the case of KGeP, where cation vacancies (V_K) are also the lowest-energy acceptors.

band gap of RbSnBi (Rb is more electropositive than K). Again, as in the case of KSnBi, RbSnBi is natively doped n-type due to the low formation energy of the anti-site Bi_{Sn} defect under Rb-rich growth conditions, with predicted free electron concentration of 8.6×10^{19} cm^{-3}, assuming 500 °C growth temperature.

NaGeP. NaGeP is a relatively larger band gap ABX phase compared to KSnSb, KSnBi, and RbSnBi since it is composed of more electronegative pnictide (P). However, the native defects in NaGeP (Fig. 7d) exhibit behavior similar to those in KSnSb, KSnBi, and RbSnBi. For example, under Na-rich conditions, which maximizes ΔE_{don}, the lowest-energy acceptor is the anti-site defect Ge_P while P_{Ge} is the lowest-energy native donor. The largest n-type dopability window ΔE_{don} is ~0.17 eV under Na-rich conditions; consequently, NaGeP is an n-type dopable ABX phase. However, a key qualitative difference is that the anti-site Ge_P is a deep defect, compared to Sn_{Sb} and Sn_{Bi} (Fig. 7a–c), which are shallow defects. This could be a direct

consequence of the significantly larger band gap of NaGeP. Defects in small band gap materials are generally shallow defects while deep defects are typically encountered in materials with larger band gaps.

KGeP. In KGeP, the native defect energetics (Fig. 7e) are such that ΔE_{don} is negative, even under the most favorable K-rich growth conditions. Since K is more electropositive than Na, the band gap of KGeP is larger than that of NaGeP. Interestingly, the lowest energy acceptors in KGeP are not only the anti-sites Ge_P but also the more commonly encountered, cation vacancies (V_K). The low formation energies of both Ge_P and V_K results in negative ΔE_{don} – even with extrinsic doping the equilibrium Fermi energy cannot exceed the point V_K intersects the $\Delta H_{D,q}$ = 0 eV line ($\sim$160 meV from the conduction band minimum). Since ΔE_{don} is not a large negative number, it may still be possible to dope KGeP n-type to 10^{17}–10^{18} cm^{-3} free electron concentrations, provided a suitable extrinsic dopant can be identified.

In summary, we find that four out of the five candidate ABX Zintl phases (KSnSb, KSnBi, RbSnBi, NaGeP, KGeP) considered for defect calculations are n-type dopable. KSnBi and RbSnBi are natively doped n-type under K-rich conditions. In general, we observe that in these five ABX phases, the lowest-energy acceptors are anti-site B_X defects under A-rich conditions, which is unlike other well-known Zintl phases where the lowest-energy acceptors are cation vacancies. The identification of n-type dopable ABX phases provides further confidence in the CRISP approach to discovering previously unknown Zintl phases with desired thermoelectric performance and doping behavior. We also observe from the defect diagrams in Fig. 7 that the relevant lowest energy defects in ABX Zintl phases are B_X and X_B anti-sites; n-type dopability is determined by their relative formation energetics. Therefore, it may be possible to gauge the n-type dopability of all 17 new ABX phases (in KSnSb structure) by calculating the defect energetics of only B_X and X_B anti-site defects.

4 Conclusions

Computational discovery of novel functional materials is often: (1) focused on known materials reported in crystallographic databases, and (2) hampered by the lack of the desired doping behavior of the candidate materials. Prediction of material dopability on a large scale remains challenging. In this regard, first-principles defect calculations are useful in assessing dopability of materials but the associated high computational cost make them prohibitive for large-scale explorations. In this work, we show that the chemical replacements in structure prototype (CRISP) approach offers new opportunities to explore previously unknown compounds with desired functional performance and doping behavior. Using materials that already exhibit the desired properties as structural prototypes increases the likelihood of discovering new promising compounds. We apply the CRISP approach to discover new ABX Zintl phases that adopt the KSnSb structure type, exhibit high TE performance and are potentially n-type dopable. While we have demonstrated the application of CRISP approach to discover n-type Zintl phases for thermoelectrics, the approach can be extended to the discovery of new compounds for other applications with designed properties and dopability.

Conflicts of interest

There are no conflicts to declare.

Acknowledgements

PG and VS acknowledge support from NSF DMR program, grant no. 1729594. AJ, AF, and AG were funded by the U.S. Department of Energy, Office of Basic Energy Sciences, Early Career Research Program. The research was performed using computational resources sponsored by the Department of Energy's Office of Energy Efficiency and Renewable Energy and located at the NREL. This research used resources of the National Energy Research Scientific Computing Center (NERSC), a DOE Office of Science User Facility supported by the Office of Science of the U.S. Department of Energy. Work at the Lawrence Berkeley National Laboratory was supported under Contract No. DE-AC02-05CH11231.

References

1 R. Nesper, *Angew. Chem., Int. Ed. Engl.*, 1991, **30**, 789.
2 H. Schäfer, *Annu. Rev. Mater. Sci.*, 1985, **15**, 1.
3 R. Nesper, *Z. Anorg. Allg. Chem.*, 2014, **640**, 2639.
4 S. C. Sevov, *Zintl Phases*, John Wiley & Sons Ltd, 2002, ch. 6, p. 113.
5 W. Klemm, *Trab. Reun. Int. React. Solidos, 3rd*, 1957, **2**, 447.
6 W. Klemm, *Proc. Chem. Soc., London*, 1959, 329–364, DOI: 10.1039/PS9580000329.
7 I. R. Fisher, S. L. Bud'ko, C. Song, P. C. Canfield, T. C. Ozawa and S. M. Kauzlarich, *Phys. Rev. Lett.*, 2000, **85**, 1120.
8 S.-J. Kim, J. R. Ireland, C. R. Kannewurf and M. G. Kanatzidis, *J. Solid State Chem.*, 2000, **155**, 55.
9 E. S. Toberer, C. A. Cox, S. R. Brown, T. Ikeda, A. F. May, S. M. Kauzlarich and G. J. Snyder, *Adv. Funct. Mater.*, 2008, **18**, 2795.
10 R. Marchand and W. Jeitschko, *J. Solid State Chem.*, 1978, **24**, 351.
11 A. Zevalkink, W. G. Zeier, G. Pomrehn, E. Schechtel, W. Tremel and G. J. Snyder, *Energy Environ. Sci.*, 2012, **5**, 9121.
12 E. S. Toberer, A. Zevalkink, N. Crisosto and G. J. Snyder, *Adv. Funct. Mater.*, 2010, **20**, 4375.
13 B. R. Ortiz, P. Gorai, L. Krishna, R. Mow, A. Lopez, R. McKinney, V. Stevanovic and E. S. Toberer, *J. Mater. Chem. A*, 2017, **5**, 4036.
14 J. Zhang, L. Song, G. K. H. Madsen, K. F. F. Fischer, W. Zhang, X. Shi and B. B. Iversen, *Nat. Commun.*, 2016, **7**, 1.
15 B. Ortiz, P. Gorai, V. S. Stevanović and E. S. Toberer, *Chem. Mater.*, 2017, **29**, 4523.

16 *Computational Materials Discovery*, ed. A. R. Oganov, G. Saleh and A. G. Kvashnin, The Royal Society of Chemistry, 2018, pp. 1–455, DOI: 10.1039/9781788010122.
17 S. Curtarolo, G. L. Hart, M. B. Nardelli, N. Mingo, S. Sanvito and O. Levy, *Nat. Mater.*, 2013, **12**, 191.
18 G. Hautier, A. Jain and S. P. Ong, *J. Mater. Sci.*, 2012, **47**, 7317.
19 A. Jain, Y. Shin and K. A. Persson, *Nat. Rev. Mater.*, 2016, **1**, 1.
20 P. Gorai, V. Stevanovic and E. S. Toberer, *Nat. Rev. Mater.*, 2017, **2**, 1.
21 L. Yu and A. Zunger, *Phys. Rev. Lett.*, 2012, **108**, 068701.
22 G. Ceder, G. Hautier, A. Jain and S. Ong, *MRS Bull.*, 2011, **36**, 185.
23 N. Mounet, M. Gibertini, P. Schwaller, D. Campi, A. Merkys, A. Marrazzo, T. Sohier, I. E. Castelli, A. Cepellotti and G. Pizzi, *et al.*, *Nat. Nanotechnol.*, 2018, **13**, 246.
24 R. Gautier, X. Zhang, L. Hu, L. Yu, Y. Lin, T. O. Sunde, D. Chon, K. R. Poeppelmeier and A. Zunger, *Nat. Chem.*, 2015, **7**, 308.
25 X. Zhang, L. Yu, A. Zakutayev and A. Zunger, *Adv. Funct. Mater.*, 2012, **22**, 1425.
26 B. Meredig, A. Agrawal, S. Kirklin, J. E. Saal, J. W. Doak, A. Thompson, K. Zhang, A. Choudhary and C. Wolverton, *Phys. Rev. B: Condens. Matter Mater. Phys.*, 2014, **89**, 094104.
27 C. E. Wilmer, M. Leaf, C. Y. Lee, O. K. Farha, B. G. Hauser, J. T. Hupp and R. Q. Snurr, *Nat. Chem.*, 2012, **4**, 83.
28 Y. Hinuma, T. Hatakeyama, Y. Kumagai, L. A. Burton, H. Sato, Y. Muraba, S. Iimura, H. Hiramatsu, I. Tanaka and H. Hosono, *et al.*, *Nat. Commun.*, 2016, **7**, 1.
29 E. D. Cubuk, A. D. Sendek and E. J. Reed, *J. Chem. Phys.*, 2019, **150**, 214701.
30 M. R. Filip and F. Giustino, *J. Phys. Chem. C*, 2016, **120**, 166.
31 J. Yan, P. Gorai, B. Ortiz, S. Miller, S. A. Barnett, T. Mason, V. Stevanovic and E. S. Toberer, *Energy Environ. Sci.*, 2015, **8**, 983.
32 S. Huang, H. J. Liu, D. D. Fan, P. H. Jiang, J. H. Liang, G. H. Cao, R. Z. Liang and J. Shi, *J. Phys. Chem. C*, 2018, **122**, 4217.
33 G. Xing, J. Sun, Y. Li, X. Fan, W. Zheng and D. J. Singh, *Phys. Rev. Mater.*, 2017, **1**, 065405.
34 G. Trimarchi, X. Zhang, M. J. DeVries Vermeer, J. Cantwell, K. R. Poeppelmeier and A. Zunger, *Phys. Rev. B: Condens. Matter Mater. Phys.*, 2015, **92**, 165103.
35 C. Barreteau, J.-C. Crivello, J.-M. Joubert and E. Alleno, *Comput. Mater. Sci.*, 2019, **156**, 96.
36 R. Belghit, H. Belkhir, M. Kadri, D. Heciri, M. Bououdina and R. Ahuja, *Phys. B*, 2018, **545**, 18.
37 A. Belsky, M. Hellenbrandt, V. L. Karen and P. Luksch, *Acta Crystallogr., Sect. B: Struct. Sci.*, 2002, **58**, 364.
38 G. Kresse and J. Furthmüller, *Phys. Rev. B: Condens. Matter Mater. Phys.*, 1996, **54**, 11169.
39 J. P. Perdew, K. Burke and M. Ernzerhof, *Phys. Rev. Lett.*, 1996, **77**, 3865.
40 P. Gorai, A. Goyal, E. S. Toberer and V. Stevanović, *J. Mater. Chem. A*, 2019, **7**, 19385.
41 S. P. Ong, W. D. Richards, A. Jain, G. Hautier, M. Kocher, S. Cholia, D. Gunter, V. L. Chevrier, K. A. Persson and G. Ceder, *Comput. Mater. Sci.*, 2013, **68**, 314–319.
42 A. Jain, S. P. Ong, W. Chen, B. Medasani, X. Qu, M. Kocher, M. Brafman, G. Petretto, G.-M. Rignanese and G. Hautier, *et al.*, *Concurr. Comp.-Pract. E.*, 2015, **27**, 5037–5059.
43 K. Mathew, J. H. Montoya, A. Faghaninia, S. Dwarakanath, M. Aykol, H. Tang, I.-h. Chu, T. Smidt, B. Bocklund and M. Horton, *et al.*, *Comput. Mater. Sci.*, 2017, **139**, 140–152.
44 A. Jain, G. Hautier, S. P. Ong, C. J. Moore, C. C. Fischer, K. A. Persson and G. Ceder, *Phys. Rev. B: Condens. Matter Mater. Phys.*, 2011, **84**, 045115.
45 G. Hautier, S. P. Ong, A. Jain, C. J. Moore and G. Ceder, *Phys. Rev. B: Condens. Matter Mater. Phys.*, 2012, **85**, 155208.
46 S. P. Ong, L. Wang, B. Kang and G. Ceder, *Chem. Mater.*, 2008, **20**, 1798.
47 G. Grimvall, B. Magyari-Köpe, V. Ozoliņš and K. A. Persson, *Rev. Mod. Phys.*, 2012, **84**, 945.
48 R. W. McKinney, P. Gorai, S. Manna, E. Toberer and V. Stevanovic, *J. Mater. Chem. A*, 2018, **6**, 15828.
49 F. Birch, *J. Geophys. Res.*, 1952, **57**, 227–286.
50 S. Lany and A. Zunger, *Phys. Rev. B: Condens. Matter Mater. Phys.*, 2008, **78**, 235104.
51 S. Ohno, K. Imasato, S. Anand, H. Tamaki, S. D. Kang, P. Gorai, H. K. Sato, E. S. Toberer, T. Kanno and G. J. Snyder, *Joule*, 2017, **2**, 141.
52 P. Gorai, B. Ortiz, E. S. Toberer and V. Stevanovic, *J. Mater. Chem. A*, 2018, **6**, 13806.
53 V. Stevanović, S. Lany, X. Zhang and A. Zunger, *Phys. Rev. B: Condens. Matter Mater. Phys.*, 2012, **85**, 115104.
54 A. Goyal, P. Gorai, H. Peng, S. Lany and V. S. Stevanović, *Comput. Mater. Sci.*, 2016, **130**, 1.
55 A. Bouhemadou, S. Bin-Omran, D. Allali, S. Al-Otaibi, R. Khenata, Y. Al-Douri, M. Chegaar and A. Reshak, *Mater. Res. Bull.*, 2015, **64**, 337.
56 J. Zhang, L. Song and B. B. Iversen, *npj Comput. Mater.*, 2019, **5**, 76.
57 J. Schmidt, J. Shi, P. Borlido, L. Chen, S. Botti and M. A. L. Marques, *Chem. Mater.*, 2017, **29**, 5090.
58 L. Weston, V. Tshitoyan, J. Dagdelen, O. Kononova, A. Trewartha, K. A. Persson, G. Ceder and A. Jain, *J. Chem. Inf. Model.*, 2019, **59**, 3692.
59 D.-Y. Chung, T. Hogan, P. Brazis, M. Rocci-Lane, C. Kannewurf, M. Bastea, C. Uher and M. G. Kanatzidis, *Science*, 2000, **287**, 1024.
60 W. Li, J. Carrete, G. K. H. Madsen and N. Mingo, *Phys. Rev. B: Condens. Matter Mater. Phys.*, 2016, **93**, 205203.
61 M. Q. Arguilla, N. D. Cultrara, M. R. Scudder, S. Jiang, R. D. Ross and J. E. Goldberger, *J. Mater. Chem. C*, 2017, **5**, 11259–11266.

